

Air Pressure Impact on the Avalanche Size for Turn-to-Turn Insulation of Inverter-Fed Motors

H. Naderiallaf, Y. Ji, P. Giangrande and M. Galea

Abstract—This paper endeavours to illuminate the variations of various streamer inception parameters (SIPs) with respect to air pressure based on Schumann’s streamer inception criterion (SCSIC). The results based on measured PDIV values and using electric field distribution obtained via electrostatic simulations and ionization swarm parameters reveal that the Schumann constant, K , which is the natural logarithm of the threshold number of electrons determining the transition from Townsend to streamer discharge, and consequently, the critical avalanche size (N_c) increase with air pressure reduction. Different SIPs such as critical field line length (CFLL), effective ionization coefficient of air (α_{eff}), PD inception field (E_{inc}), firing voltage (V_{firing}) across the critical field line (CFL), K and N_c are analysed extensively as a function of air pressure. In light of the findings of this contribution, it is demonstrated that the derived K functions as a function of air pressure can improve drastically the accuracy of PDIV prediction in particular for low air pressures rather than a single K parameter value obtained at ground level. The study’s findings represent a guideline for electrical machine designers for improving the insulation design of electrical machines employed in the More Electric Aircraft (MEA) applications.

Index Terms— Air pressure, avalanche breakdown, electric machines, finite element analysis, insulation, partial discharges, reliability.

I. INTRODUCTION

PD is known as the most concerning stress factor, contributing to turn-to-turn winding insulation degradation which is the most vulnerable part of electrical machines’ insulation system. Partial discharge (PD) inception is considered as the end-of-life criterion for only organic insulating materials (Type I), such that when it occurs leads to premature failure, happening in a few days if not hours. Therefore, when wire insulation is Type I, it is necessary to design the insulation system based on PD-free criterion, i.e., the maximum peak voltage between adjacent turns should be lower than the minimum probable voltage required to incept PD activity between turns [1].

The danger of PD inception is more challenging in

insulation design for aerospace applications since air pressure reduction corresponding to high cruising altitude results in two undesirable outcomes. First, partial discharge inception voltage (PDIV) is reduced and second, the harmfulness or damage associated with PD activity is significantly increased at low air pressures [2], [3], [4]. The destructive potential of PD at high altitudes (i.e., reduced air pressures) is very considerable, such that even corona-resistant materials (i.e., Type II, mixed organic-inorganic insulation) which can withstand moderate PD activity at ground level, cannot sustain PD inception at reduced air pressures, delivering very short PD endurance time (i.e., less than one hour) [4]. This limits the increasing level of DC bus voltage in power converters, where its maximum allowed value becomes well below the voltage targets expected for the More Electric Aircraft (MEA) [2]. Therefore, it is crucial to improve the turn-to-turn insulation system by increasing the PDIV values (e.g., thicker thickness) or developing entirely novel solid insulation for MEA applications [4]. By gaining knowledge about the harmfulness or damage of PD at low air pressures, a better insulation design can be achieved (e.g., enhanced awareness in selecting the optimum insulating materials) for MEA applications. Commercial aircraft currently operate at voltages below 1 kV. However, it is widely recognized that higher operating voltages are needed to increase power density and keep conductor weight at an acceptable level for MEA. In electrical insulation technology, higher voltage levels result in greater electric tension within the insulation system [5]. This not only promotes the occurrence of partial discharges (PD) but also enhances their destructive potential [6], [7]. Although short PD endurance times have been experimentally proven even for corona-resistant insulations under low air pressures [2], [3], [4], a comprehensive model is lacking to analyse the variations of streamer inception parameters (SIPs) under such conditions and explain the observed experimental results. By addressing the research gap in the modelling of PDIV at low air pressures, this study aims to enhance the accuracy of the PDIV model based on the finite element method (FEM) proposed in [8]. Differently from [8],

This paper was submitted for review in April 2023. This work was partially supported by Project AIMS1, financed by the Malta Council for Science & Technology, for and on behalf of the Foundation for Science and Technology, through the FUSION: R&I Research Excellence Programme. (Corresponding author: Hadi Naderiallaf).

Hadi Naderiallaf is with the Power Electronics, Machine and Control Group (PEMC), The University of Nottingham, Nottingham, U.K. (e-mail: Hadi.Naderiallaf@nottingham.ac.uk).

Yatai Ji is with the Key Laboratory of More Electric Aircraft Technology of Zhejiang Province, University of Nottingham Ningbo, China, Ningbo, China. (e-mail: yatai.ji@nottingham.edu.cn).

Paolo Giangrande is with the Department of Engineering and Applied Sciences, University of Bergamo, Dalmine, Italy (e-mail: paolo.giangrande@unibg.it).

Michael Galea is with the Department of Industrial Electrical Power Conversion, University of Malta, Msida, Malta (e-mail: michael.d.galea@um.edu.mt).

where a single steady Schumann constant (K) is considered, this study proposes a K which varies as a function of the air pressure. This refinement is crucial because relying on a single K parameter obtained at ground level results in an underestimation of PDIV and may lead to a suboptimal selection of DC bus voltage for achieving a PD-free design at low air pressures. By deriving new K equations, this research enables more confident increases in DC bus voltage, consequently, facilitating the reduction of conductor weight at low air pressures.

II. N_c CALCULATION BASED ON SCSIC

Considering this presumption that streamer discharges play the main role in dielectric degradation from ground level to low air pressures, K value corresponding to streamer discharges can be calculated from (1) [9], [10], [11].

$$K = \int_0^{x_c} \alpha_{\text{eff}}(x) \cdot dx \quad (1)$$

where x is the distance from the starting point of the avalanche, x_c is the critical avalanche length along the electric field line where the discharge develops, and α_{eff} is the effective ionization coefficient of air defined as:

$$\alpha_{\text{eff}} = \alpha - \eta \quad (2)$$

where α and η are the ionization and the attachment coefficients, respectively, depending on the gas nature, electric field intensity, and the gas number density or gas pressure [11].

Fast-moving filamentary streamers emerge from an avalanche's head when it reaches a certain size of N_c [12]. Any knowledge about N_c at low air pressures can be a clue for insulation design and PD harmfulness evaluation for aerospace applications. It is possible to estimate the earliest value of N_c based on SCSIC. It is noteworthy to mention that the final avalanche size reaching the anode is proportional to the discharge magnitude. In addition, when a discharge takes place due to air dissociation and thermal dilation in the discharge area, α_{eff} can change, impacting N_c for the subsequent discharges. Therefore, the earliest value of N_c which is the critical number of electrons in a Townsend avalanche that triggers the transition to a streamer discharge is [9], [10], [11]:

$$N_c = \exp(K) \quad (3)$$

It is important to acknowledge that this study simplifies and assumes that avalanche growth is exponential from $x = 0$ to $x = x_c$ [5], [11], [13]. It is worth noting that in reality, the growth of the avalanche from the initial provision of electrons is not exponential until a mid-point $x < x_c$ is reached, at which the population of electrons becomes sufficiently large. However, this simplification does not affect other SCSIC-derived SIPs or the PDIV modelling, which rely on the maximum K value determined under PDIV rather than N_c .

To prevent a decrease in PDIV caused by residual charges from previous PD activities, each specimen is subjected to a single test. As a result, the only way to start a discharge event

is by ionising the air [8]. Moreover, it is considered that the wire's insulation is clean throughout the test campaign. It should be noted that in practical applications where pollution is present, the first electrons to initiate discharges can be released by the insulating surface. Furthermore, bipolar excitations with polarity reversal (e.g., AC waveforms) are preferred over voltage waveforms with a DC component (e.g., unipolar excitations) in order to reduce the effect of space charge accumulation on both the field distribution in the air wedge and PDIV [14].

A. Simulation of Non-Uniform Electric Field Distribution

The electric field distribution between two cylindrical insulated wires is simulated and analysed through a two-dimensional (2D) COMSOL Multiphysics® simulation based on FEM as shown in Fig. 1.

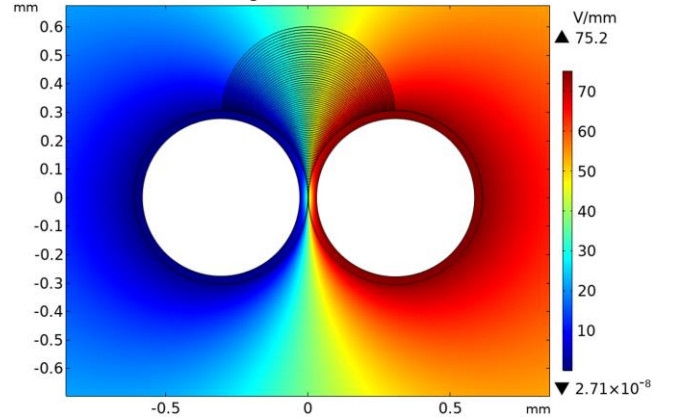


Fig. 1. Electrostatic simulation of non-uniform electric field distribution between insulated cylindrical wires using 2D COMSOL Multiphysics®.

The initial electrostatic simulations are carried out with a unitary voltage [13], considering bare wire diameter of 0.556 mm, insulation thickness of 28.5 μm and insulation permittivity of 4.31 as inputs. A reference database is obtained as outputs including 1) field line lengths only in the air wedge between the wires sorted from smallest to longest, and 2) the electric field intensity corresponding to each field line which accordingly will have a downward trend. It is noteworthy to highlight that while the former (i.e., field line lengths) remains constant with increasing voltage, only the latter is enhanced which should be calculated for each voltage level, thus updating the reference database.

The optimal number of electric field lines, n_{FL} , in the air wedge should be considered so that the distance between the field lines should not be more than 1 μm . This choice allows to guarantee an accurate determination of K at reduced air pressure. This number depends on the conductor diameter and insulation thickness and can be determined using a function introduced in [8]:

$$n_{\text{FL}}(D, s) = 2 \cdot \text{ceil}\{200 \cdot [3.922 \cdot (D + s) - 0.02597]\} \quad (4)$$

where $\text{ceil}(x)$ is a MATLAB function which rounds the x values to the nearest integer toward positive infinity. D and s are conductor diameter and insulation thickness, respectively,

expressed in mm . The obtained optimal number of field lines for the cylindrical insulated wire under investigation is 908 according to (4). It is important to highlight that the 2D domain meshing affects the precision of the field line numbers, n_{FL} , in (4) and the computed field line length. Particularly, the relationship in (4) only holds true when an extremely fine mesh size is used, as it is in the FEM simulations of this study. However, if a coarser mesh size is chosen, n_{FL} should be raised and longer field line lengths are computed. For example, if the mesh size is coarse rather than extremely fine, the n_{FL} obtained from (4) should be increased by 79. Additionally, compared to the outcomes produced with an extremely fine mesh size, the calculated shortest and longest field line lengths are respectively 178.6% and 0.84% longer when using a coarse mesh size. Thus, the mesh size has a significantly greater effect on the length calculation of shorter field lines compared to longer ones.

B. Deriving Ionization Swarm Parameters

The air ionization (α) and attachment (η) coefficients required in (2) are calculated by BOLSIG+ software using ionization swarm parameters found in the LXCAT database for dry air [15], [16]. The outputs of BOLSIG+ are α/n and η/n both in m^2 and as a function of the reduced electric field, E/n , in Townsend. n is the gas number density in m^{-3} , and E is the electric field corresponding to each field line calculated by COMSOL, governing the energy gained between two successive collisions. The gas number density is obtained through the ideal gas law, as in (5):

$$n = p \cdot V / k_B \cdot T \quad (5)$$

where p is in Pascals, V is the test volume (e.g., the vacuum chamber volume) in m^3 , k_B is the Boltzmann constant, $1.380649 \times 10^{-23} J/K$, and T is the gas absolute temperature in Kelvin. Therefore, the minimum and maximum reduced electric fields corresponding to the longest and smallest field line length are computed and used as range limits in BOLSIG+. Addition input data to BOLSIG+ are the gas temperature and composition. According to [17], dry air at room temperature (20°C) is constituted of Nitrogen (N_2), 78.08%, Oxygen (O_2), 20.95%, Argon (Ar), 0.93%, and carbon dioxide (CO_2), 0.04%. Aiming at building a well-founded dataset, the air composition is determined taking into account the humidity level, which is controlled by the test chamber throughout the experimental campaign. Therefore, the moist air composition for each combination of air pressure, temperature and humidity can be obtained from:

$$moist\ gas\ ratio(x) = dry\ gas\ ratio(x) \cdot (1 - M_{H_2O}) \quad (6)$$

where x stands for gases in air composition N_2 , O_2 , Ar, and CO_2 . The dry gas ratio for each gas is the same as the above-mentioned percentages. M_{H_2O} is the water molar concentration in air [8]:

$$M_{H_2O} = 0.622 \cdot \left(\frac{p_{H_2O}}{p - p_{H_2O}} \right) \quad (7)$$

where 0.622 is the value of the ratio between the molar masses of water (18.02) and air (28.96). p_{H_2O} is the water partial pressure in Pascals. p_{H_2O} is calculated once the relative humidity, RH , and gas temperature, t_{amb} , in °C are known from the empirical equation (8) [8]:

$$p_{H_2O} = 611 \cdot RH \cdot 10^{7.5 \left(\frac{t_{amb}}{t_{amb} + 237} \right)} \quad (8)$$

TABLE I
GAS COMPOSITIONS OF MOIST AIR IN PERCENTAGE (%)
AS A FUNCTION OF AIR PRESSURE

| Air pressure (mbar) | Ar | CO ₂ | H ₂ O | N ₂ | O ₂ |
|---------------------|------|-----------------|------------------|----------------|----------------|
| 1000 | 0.92 | 0.04 | 0.6 | 77.61 | 20.82 |
| 600 | 0.92 | 0.04 | 0.8 | 77.45 | 20.78 |
| 400 | 0.92 | 0.04 | 0.96 | 77.32 | 20.75 |
| 200 | 0.92 | 0.04 | 1.51 | 76.90 | 20.63 |
| 100 | 0.91 | 0.04 | 2.53 | 76.1 | 20.42 |

The defined gas compositions of moist air associated with different air pressure values obtained from (6) to (8) considered as inputs for BOLSIG+ are summarized in Table I. For the sake of brevity, the gas ratio numbers are reported with two decimal digits. The relative humidity (RH) is set at 13% at 40°C, 1000 mbar throughout the experiments. However, the moisture percentage slightly increases when air pressure reduces. It can be ascribed to the inevitable dehumidifying or out-gassing promotion of polyamide-imide or connection accessories (e.g., cables) at low air pressures. This relies on the principle that gas solubility (i.e., gas moisture) decreases as air pressure is reduced (Henry's law); when polyamide-imide or cable connections are held under vacuum, dissolved gas moisture will come out of insulation bulk [18].

C. Calculation of K and N_c

The following algorithm, [13], is implemented in MATLAB to calculate the empirical value of K corresponding to each air pressure:

- 1) Import the field line lengths database in mm as a function of the electric field simulated by COMSOL for unitary voltage, $E_{database}(x, y)$ in V/m .
- 2) Determine the field between the two insulated wires under PDIV by linearity considering the measured peak value of PDIV as:

$$E(x, y) = PDIV \cdot E_{database}(x, y) \quad (9)$$

- 3) Import the database of α_{eff}/n in m^2 as a function of reduced electric field, E/n , (Townsend), from BOLSIG+. The units of the outputs need to be modified as:

$$3-1 \text{ Convert Townsend to electric field in } V/m \text{ from (10):} \\ E(V/m) = n \cdot Townsend \cdot 10^{-21} \quad (10)$$

$$3-2 \text{ Convert } \alpha_{eff}/n \text{ in } m^2 \text{ to } \alpha_{eff} \text{ in } mm^{-1} \text{ from (11):} \\ \alpha_{eff}(mm^{-1}) = n \cdot \alpha_{eff}/n \cdot 10^{-3} \quad (11)$$

- 4) Using the database imported in step 3), calculate α_{eff} in mm^{-1} for each field line while accounting for the electric field

strength of the field line under PDIV from step 2).

5) For all field line numbers, n_{FL} , calculate the right term in (1).

6) Select the maximum K value determined in step (5) and record it as the experimental K that is used in the SCSIC to estimate PDIV.

7) After finding K , the earliest value of N_c is calculated from (3). The field line length along which the highest value of K is achieved is reported as CFLL.

III. EXPERIMENTAL TESTS CAMPAIGN

It is indispensable to have experimental data to ascertain the correct value of K as a function of air pressure. Therefore, PD tests are performed to obtain PDIV at different air pressures. In the following subsections, first, the test samples are introduced. Second, the method to measure bare wire diameter, insulation thickness and relative permittivity is explained. Then, the PD measurement setup and test procedure are described.

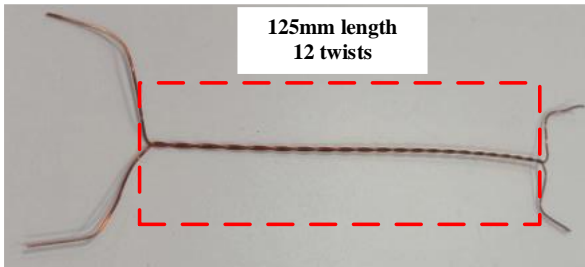


Fig. 2. Picture of a TPs used for investigation.

TABLE II
ENAMELLED MAGNET WIRE SPECIFICATIONS

| Parameter | Value |
|---------------------------|-----------------|
| Thermal class | 220°C |
| Bare copper wire diameter | 0.556 mm |
| Insulation thickness | 28.5 μ m |
| Relative permittivity | 4.31 |
| Insulation grade | Grade II |
| Insulation basecoat | Polyester-imide |
| Insulation overcoat | Polyamide-imide |

A. Test Samples for PDIV Tests

The test samples are twisted pairs (TPs) manufactured out of grade 2 round enamelled wires to model the turn-to-turn insulation of winding which is the most vulnerable part of the insulation system in electrical machines. The bare copper wire diameter and insulation thickness are 0.556 mm and 28.5 μ m, respectively. The wires insulation features a polyamide-imide and a THEIC-modified polyester-imide layers as overcoat and basecoat, respectively, categorized in the thermal class of 220°C. The wires are twisted 12 times while the load tension of 7 N is applied during twisting for TPs construction [19]. Five pristine TPs are used to measure PDIV for each air pressure. Each test sample is tested only once and discarded after each test. It is necessary to prevent the possibility of PDIV drop resulting from damage caused by previous PD activities [20]. For each considered air pressure, both the averaged of measured PDIV values (i.e., $PDIV_{mean}$) and 10th percentile (B10) of the 2-parameter Weibull distribution fitted to the dataset of five TPs

(i.e., $PDIV_{B10}$) are calculated to be employed for K calculations. Fig. 2 shows a typical test specimen and Table II reports the cylindrical enamelled magnet wire specifications.

B. Measuring Bare Wire Diameter, Insulation Thickness, and Relative Permittivity

The inputs for the COMSOL model in Fig. 1 are bare copper wire diameter, insulation thickness and wire insulation relative permittivity. The first two dimensions reported in Table II are the averaged measured values for 20 cylindrical wires using a micrometre screw with an accuracy of 1 μ m. To measure the bare copper wire diameter, the wire is stripped by a laser wire stripping machine, in order to remove the insulation without eroding the copper surface. The insulation thickness is calculated by differencing the measured wire diameters before and after the insulation removal. The relative permittivity of wire insulation is determined by measuring the capacitance of a 10 cm cylindrical wire piece at 50 Hz using a sinusoidal voltage waveform generated through a Megger Delta4000. The apparent capacitance is obtained by stripping the wire from one end so that it can be connected to the Megger, while the middle part is painted with conductive paint with a length of 10 cm to create the ground electrode [8]. The insulation capacitance is recorded within the voltage range from 20 V to 100 V with steps of 20 V at 40°C (the same temperature as used for PDIV tests). For each applied voltage, the average capacitance is used to compute the relative permittivity, ϵ_r , using (12):

$$\epsilon_r = \frac{C_{wire}}{2\pi\epsilon_0 l_{painted}} \cdot \ln\left(\frac{D_{insulated}}{D_{stripped}}\right) \quad (12)$$

where C_{wire} , ϵ_0 , $l_{painted}$, $D_{insulated}$ and $D_{stripped}$ are the wire capacitance, permittivity of free space, wire's painted part length, the diameter of insulated wire, and diameter of the stripped wire, respectively. Table II reports the mean measured permittivity values for 20 cylindrical insulated wires, while the averaged apparent capacitance is 245.65 pF.

C. Measurement Setup

The experimental setup employed for PD measurements is shown in Fig. 3 and schematized in Fig. 4. A set of five specimens are inserted inside a vacuum chamber with a volume of 0.064 m³ which allows precise control of air pressure. The electric heating element controlled by the industrial temperature control system is used to heat the chamber and the humidity inside the chamber is monitored through the MIAO XIN TH10S-B-H humidity sensor. The wire connections of the temperature control system and humidity sensor are enabled through the low voltage (LV) pass-through of the chamber. The Megger 4110 is used for PD investigation and the excitation voltage is detected through PICO® TA044 high voltage (HV) differential probe (70 MHz bandwidth, 1000:1 voltage ratio, 10 M Ω impedance) and displayed on the KEYSIGHT® DSOX2024A scope. PD detection is performed with a conventional indirect circuit with its schematic drawing depicted in Fig. 4. A PD-free 4.7 nF coupling capacitor is

connected in parallel with the test specimen to amplify the PD signal and improve the detection sensitivity. The PD sensor to acquire the PD pulses is a ferrite-core high-frequency current transformer (HFCT) with 0.3-100 MHz bandwidth manufactured by Kanggaote (KGT) [21].

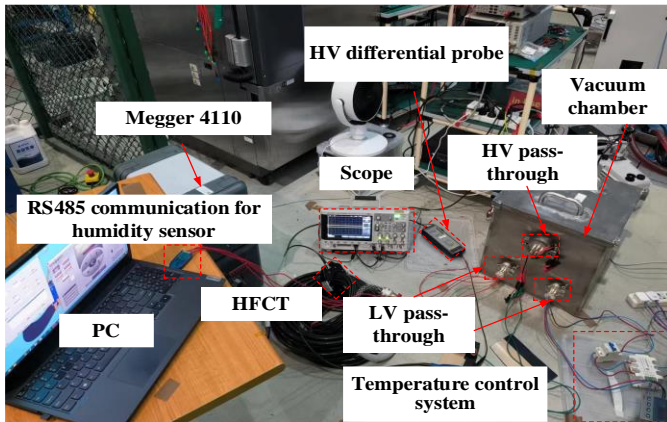


Fig. 3. Experimental test setup.

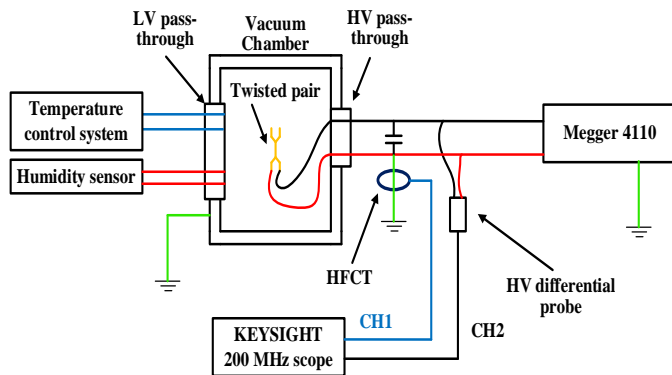


Fig. 4. Scheme of the experimental test setup.

D. Measurement Procedure

The PDIV measurements are carried out at a constant temperature of 40°C and at different air pressures: 1000, 600, 400, 200, and 100 mbar. It is important to note that in real aerospace applications, the temperature and humidity can vary. However, these parameters are kept at constant levels throughout the test campaign since this study specifically focuses on investigating the influence of air pressure on PDIV and SIPs. The reason to conduct the PDIV tests at 40°C rather than room temperature (i.e., 20°C) is to achieve a more stable humidity level and perform the PD tests at a lower humidity level. Indeed, the focus of this study is investigating the impact of air pressure on PDIV, and the PDIV dispersion level can increase with humidity raise. During the tests, the humidity is monitored perpetually and set at the desired absolute humidity (AH) level of 6.65 g/m³, corresponding to the relative humidity (RH) of 13% at 40°C, 1000 mbar [2].

To measure PDIV for each test specimen, the voltage peak is increased in steps of 10 V, whose waiting durations become longer as air pressure reduces (Table III). These durations were selected based on the proposed time intervals in [22]. This decision results from the fact that a PD can only be incepted

when two requirements are met: (1) a voltage greater than the PDIV; and (2) the availability of a free electron. Free electrons are produced by photoionization of the gas molecules [23]. The chance of photoionization diminishes due to the decrease in gas density at reduced air pressures. Hence, it is important to consider that when the rate of voltage rise exceeds a certain threshold, free electrons can emerge after reaching the PDIV. This occurrence may lead to a notable positive error in the measured PDIV, in particular, at low air pressures [22].

TABLE III

WAITING DURATION OF VOLTAGE STEPS CONSIDERED FOR PDIV TESTS AS A FUNCTION OF AIR PRESSURE.

| Air pressure (mbar) | 1000 | 600 | 400 | 200 | 100 |
|---------------------|------|-----|-----|-----|-----|
| Duration (min) | 0.5 | 1 | 2 | 4 | 6 |

IV. RESULTS AND DISCUSSIONS

A. PDIV

Fig. 5 and Table IV report the measured peak value of PDIV under AC 50 Hz excitation (both mean value and B10) as a function of air pressure.

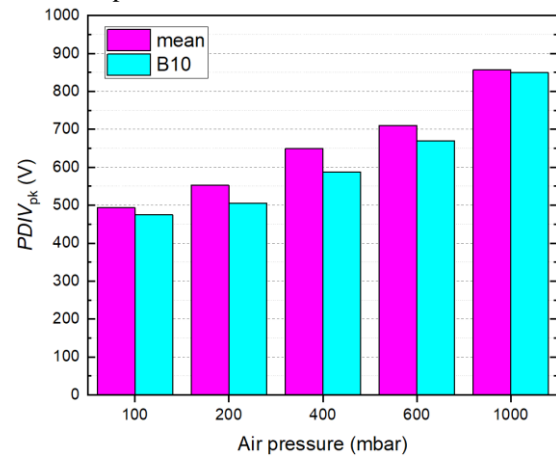


Fig. 5. Measured PDIV peak under AC 50 Hz excitation as a function of air pressure.

TABLE IV

MEASURED MEAN AND B10 OF PDIV PEAK UNDER AC 50 HZ EXCITATIONS RELEVANT TO FIG. 5.

| Air pressure (mbar) | 100 | 200 | 400 | 600 | 1000 |
|--------------------------|-------|-------|-------|-------|-------|
| PDIV _{mean} (V) | 493.3 | 552.7 | 648.8 | 710.5 | 856.4 |
| PDIV _{B10} (V) | 474.9 | 506.1 | 588 | 670.3 | 848.9 |

SIPs and PDIV estimation are performed using more than one percentile of PDIV, i.e., the PDIV mean measured peak values (PDIV_{mean}) and the B10 of the PDIV peak (PDIV_{B10}). This choice follows two main goals firstly, the evaluation of SIPs trends vs air pressure relying on more than one PDIV percentile, and secondly, to demonstrate which K value (i.e., based on PDIV_{mean} or PDIV_{B10}) provides a better PDIV prediction as a function of air pressure. It is worthwhile to recall that to conduct the qualification tests for the turn-to-turn insulation, the IEC [1] permits PDIV tests on twisted-pair samples using either sinusoidal or impulse voltages. The PDIV

values are lower under sinusoidal excitations with rise times shorter than $1 \mu\text{s}$ [24]. Even when measured with a 50 Hz sinusoidal supply, the results remain equivalent, providing a slightly more conservative evaluation of PDIV for turn-to-turn insulation under the 2-level inverter or surge generator excitations [4], [25]. Comparative PDIV tests conducted on twisted pairs in [26] demonstrated that AC excitations yield the lowest PDIV values compared to PWM. Considering these findings, a conservative approach is taken in this investigation, performing PDIV measurements under AC 50 Hz excitations.

Fig. 5 shows that PDIV drops with air pressure reduction as expected which is due to the lower gas density, providing a longer mean free path for an electron during the discharging process, implying an increase of the mean kinetic energy of electrons, thus the PD inception can occur at a lower electric field as air pressure decreases [2]. Considering MEA applications (e.g., air pressure of 200 mbar corresponding to cruising altitude of 11.8 km), PDIV_{B10} is 59.61% lower than 1000 mbar.

B. CFL

Fig. 6 shows the found CFL along which the maximum value of K is obtained at different air pressures under B10 of measured PDIV through the FEM-based approach.

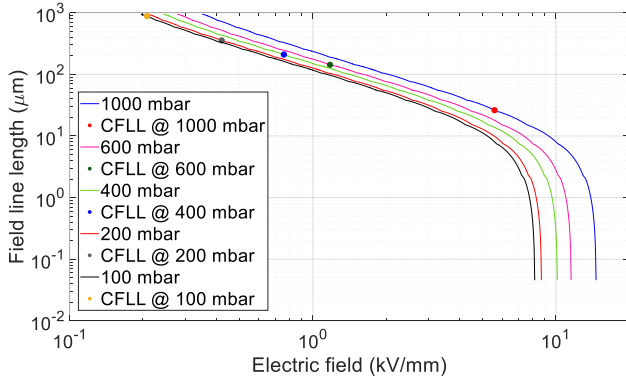


Fig. 6. Variation of CFL with air pressure based on B10 of measured PDIV using FEM-based approach.

Considering the wire's insulation thickness under investigation, it should be noted that at reduced air pressures down to 100 mbar, the highest found value of K always belongs to the electric field lines drawn from the contact point of the two insulated wires to the centre of the two circumferences (Fig. 1). As a result, the considered field lines in the air wedge simulated in Fig. 1 are sufficient to produce the electric field database for the PDIV prediction and SIPs analysis down to 100 mbar. Thus, it is not necessary to take into account the external field lines, i.e., beyond the centre of the two circumferences. Fig. 6 clarifies that the obtained CFL at 100 mbar moves close to the lowest field intensity, corresponding to the longest field line length simulated in Fig. 1.

Fig. 7 reports the acquired CFL values with respect to air pressure based on both mean measured values of PDIV ($\text{PDIV}_{\text{mean}}$) and B10 of PDIV (PDIV_{B10}).

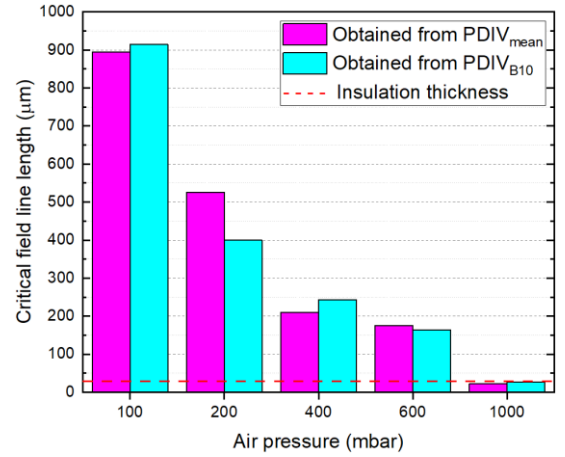


Fig. 7. CFL as a function of air pressure obtained from $\text{PDIV}_{\text{mean}}$ and PDIV_{B10} . (The dashed red lines indicate the wire insulation thickness)

Fig. 7 demonstrates that CFL increases conspicuously with air pressure reduction becoming higher than the insulation thickness. For instance, it is about 35 and 15 times longer at 100 and 200 mbar, respectively, than 1000 mbar when PDIV_{B10} is considered. As shown in Fig. 8, there is a critical region of α_{eff} curves where the α_{eff} corresponding to the critical field line (CFL) is always found in that decisive zone. This region moves towards lower electric field magnitudes, thus longer field lines, at reduced air pressures. This can explain the reason to attain a longer CFL at a lower air pressure.

Considering two assumptions, namely, (a) assuming the relative permittivity of air to be 1, and (b) considering constant and perpendicular electric fields with respect to the dielectric surface, the electric field within the gas can be expressed as $E_{\text{air}} = \epsilon_r \cdot E_{\text{Insul}}$, where ϵ_r represents the relative permittivity of the solid insulation. E_{air} and E_{Insul} correspond to the electric fields within the gas and the solid insulation, respectively. Considering l_{Insul} as the insulation thickness, the applied voltage (PDIV) is divided or allocated between the air and the solid insulation as follows:

$$\text{PDIV} = (\epsilon_r \cdot E_{\text{Insul}}) \times \text{CFL} + E_{\text{Insul}} \times l_{\text{Insul}} \quad (13)$$

Then, the voltage across the solid insulation ($V_{\text{Insul}} = E_{\text{Insul}} \times l_{\text{Insul}}$) which is measured by HV differential probe is given by:

$$V_{\text{Insul}} = \text{PDIV} \cdot \left(\frac{l_{\text{Insul}}}{\epsilon_r \cdot \text{CFL} + l_{\text{Insul}}} \right) \quad (14)$$

Considering (14), the significant increase of CFL vs insulation thickness (i.e., the red dashed line in Fig. 7, l_{Insul}) at low air pressures results in $V_{\text{Insul}} < \text{PDIV}$ which is less tangible at atmospheric pressure (i.e., 1000 mbar). Consequently, once the PD occurs at reduced air pressures, the measured voltage across the specimen (i.e., solid insulation) drops noticeably. Therefore, it is suggested the measured voltage just before PD inception (i.e., during the waiting time) to be recorded as PDIV rather than the voltage after PD occurrence when the voltage drops more outside the insulation

(i.e., in air) at low air pressures. Furthermore, it becomes evident from (14) and Fig. 7 that the diminished PDIV sensitivity to variations in enamel thickness leads to conspicuously comparable measured PDIV values for wires with different grades (i.e., insulation thicknesses) at reduced air pressures [21].

C. Effective Ionization Coefficient of Air (α_{eff})

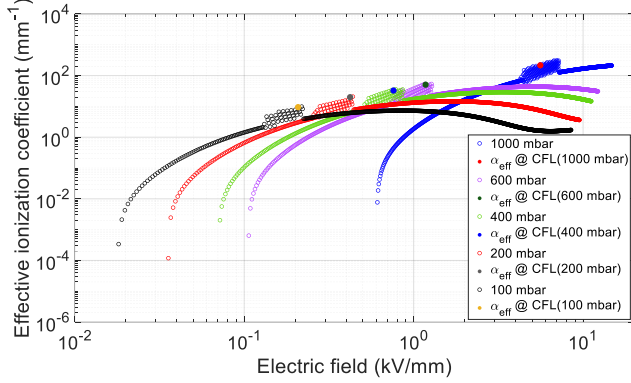


Fig. 8. α_{eff} at CFL corresponding to a specific air pressure from B10 of PDIV from the shortest field line (E_{max}) to the longest one (E_{min}) derived by BOLSIG+ using ionization swarm parameters.

Fig. 8 shows the derived effective α_{eff} associated with CFL satisfying SCSIC using BOLSIG+ based on the ionization swarm parameters found in the LXCAT database [15], [16]. It also elucidates the global α_{eff} variations of air at different air pressures as a function of electric field ranging from the E_{max} (corresponding to the shortest field line) to the E_{min} (corresponding to the longest field line). It shows the derived α_{eff} corresponding to CFL under B10 of PDIV excitation from 1000 mbar (ground level) to 100 mbar. According to Fig. 8's outcomes, α_{eff} of air corresponding to higher electric fields decreases as air pressure drops. The opposite holds for α_{eff} of air at low electric fields where it rises at reduced air pressures. In addition, Fig. 8 shows that there is a critical region or swollen area for α_{eff} of air with respect to the electric field and air pressure at which the α_{eff} dispersion becomes significantly higher at a specific electric field. This critical region has a decisive role in determining the CFL and its matching α_{eff} since the maximum value of K is always found in this region. This critical zone moves towards lower electric field values with respect to air pressure reduction, resulting in diminishing α_{eff} and an increase in the length of CFL at low air pressures.

As the air pressure decreases, as shown in Fig. 8, α_{eff} moves towards the upper boundary of the critical region, indicating a higher α_{eff} in that zone. Additionally, as the air pressure decreases, this zone becomes less dense. This means that, at low air pressures, there is a reduced likelihood of achieving a match between the field line length and α_{eff} to generate the necessary K for initiating PD inception under a specific applied voltage. Consequently, it is justifiable to expect a longer waiting time during the voltage-increasing steps when measuring PDIV at

low air pressures compared to ground level (as indicated in Table III).

Fig. 9 reports the derived α_{eff} relevant to CFL as a function of air pressure based on both measured mean values of PDIV ($\text{PDIV}_{\text{mean}}$) and B10 of PDIV (PDIV_{B10}). Fig. 9 indicates that α_{eff} drastically decreases at reduced air pressure. For example, α_{eff} is about 27 and 18 times weaker at 100 and 200 mbar, respectively, than 1000 mbar if the $\text{PDIV}_{\text{mean}}$ is taken into account. However, a lower value of α_{eff} at low air pressures cannot lead to a higher PDIV, due to the significantly longer CFL (Fig. 7). Indeed, the electron will feature a sufficient kinetic energy to create N_c even when exposed to a weaker electric field (Fig. 10). Therefore, the role of longer CFLs is more decisive than α_{eff} in determining the PDIV in low air pressure environment.

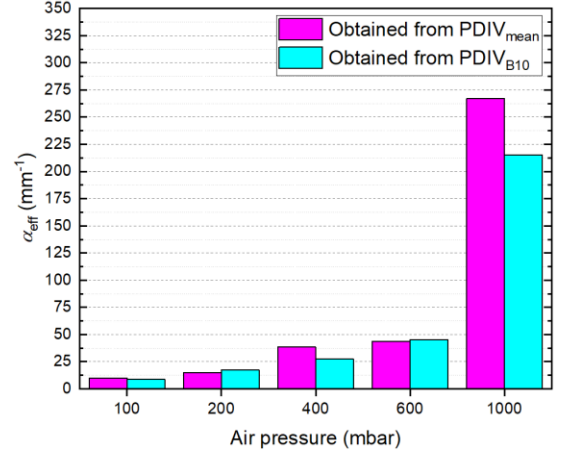


Fig. 9. α_{eff} corresponding to CFL as a function of air pressure obtained from $\text{PDIV}_{\text{mean}}$ and PDIV_{B10} .

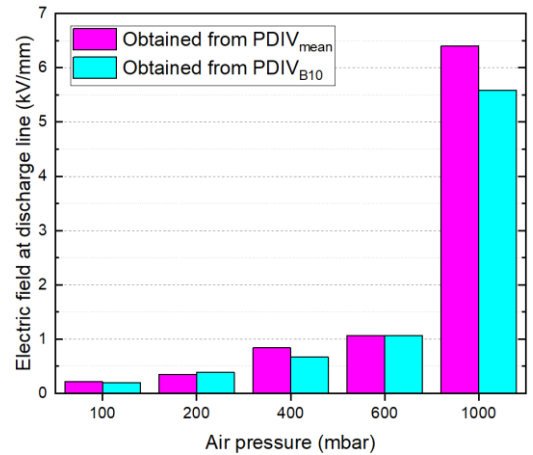


Fig. 10. Discharge field as a function of air pressure obtained from $\text{PDIV}_{\text{mean}}$ and PDIV_{B10} .

D. Discharge Electric Field

Fig. 10 presents the variation of the discharge field, E_{inc} , (i.e., electric field intensity corresponding to CFL) with respect to air pressure under PDIV. The discharge field steadily decreases with air pressure reduction highlighting a good correlation with α_{eff} (Fig. 9). Considering the $\text{PDIV}_{\text{mean}}$, E_{inc} is

about 30 and 19 times weaker at 100 and 200 mbar, respectively than 1000 mbar.

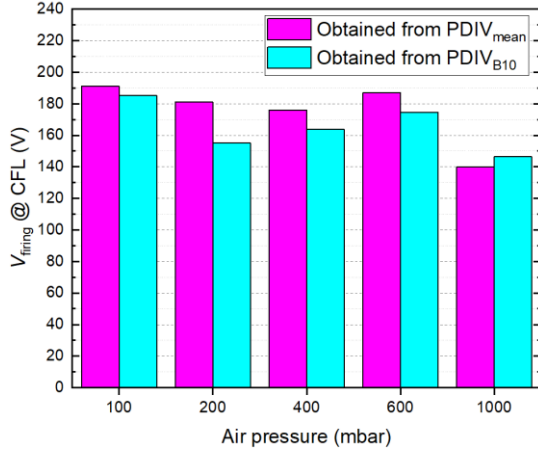


Fig. 11. Firing voltage at CFL as a function of air pressure obtained from $\text{PDIV}_{\text{mean}}$ and PDIV_{B10} .

E. Firing Voltage

Another SIP is the firing voltage, V_{firing} , which is defined as the voltage across the CFL. It can be obtained simply by multiplication of the E_{inc} reported in Fig. 10 to its correspondent CFLL quantified in Fig. 7. Fig. 11 reveals that V_{firing} remains almost stable around 184 V from 600 to 100 mbar based on $\text{PDIV}_{\text{mean}}$ while it is slightly higher at reduced air pressures than ground level. Considering the obtained V_{firing} based on PDIV_{B10} , it is only 1.26 and 1.06 times stronger at 100 and 200 mbar, respectively, than 1000 mbar. Therefore, interestingly, V_{firing} variations as a function of air pressure can be neglected compared to CFLL, α_{eff} and E_{inc} which change significantly.

F. Schumann Constant (K)

Fig. 12 elucidates that K overall increases with the air pressure decrease, getting about 1.5 and 1.3 times higher at 100 and 200 mbar, respectively, than 1000 mbar if the $\text{PDIV}_{\text{mean}}$ is considered. Indeed, as the air pressure reduces, CFLL experiences an increase (Fig. 7), while α_{eff} undergoes a decrease (Fig. 9). The rise in the fitting parameter K at low air pressures (Fig. 12) signifies that the influence of CFLL elevation in such conditions outweighs the impact of α_{eff} reduction.

It is noteworthy to introduce regression line equations fitted to K as a function of air pressure based on the validity ranges of $p \cdot d$ parameter in $\text{mbar} \cdot \text{mm}$:

$$\begin{aligned} K_{\text{mean}}(p) &= -0.003 \cdot p + 9.0432, \\ 21.87 \leq p \cdot d \leq 105.33 \text{ mbar} \cdot \text{mm} \end{aligned} \quad (15)$$

$$\begin{aligned} K_{\text{B10}}(p) &= -0.0021 \cdot p + 7.9754, \\ 26.18 \leq p \cdot d \leq 98.36 \text{ mbar} \cdot \text{mm} \end{aligned} \quad (16)$$

where $K_{\text{mean}}(p)$ and $K_{\text{B10}}(p)$ are introducing K as a function of air pressure obtained from $\text{PDIV}_{\text{mean}}$ and PDIV_{B10} , respectively, p is air pressure in mbar , and d is the CFLL obtained from the above-mentioned approach (Fig. 7) but in mm . The introduced ranges for $p \cdot d$ in (15) and (16) characterize the typical cases as the air wedges (Fig. 1) in turn-

to-turn winding insulation systems. The coefficient of determinations, R^2 , corresponding to (15) and (16) are equal to 0.86 and 0.64, respectively. This demonstrates that (15) is more reliable than (16), predicting 86% of the variance in K with respect to air pressure. Table V reports the experimental values of K as a function of air pressure associated to Fig. 12. The calculated values of $p \cdot d$ in $\text{mbar} \cdot \text{mm}$ corresponding to each air pressure level are also summarized in Table V. It is worthwhile to mention that the shape of the turn-to-turn geometry, whether it is flat or rounded, almost has no effect on the fitting parameter K [27].

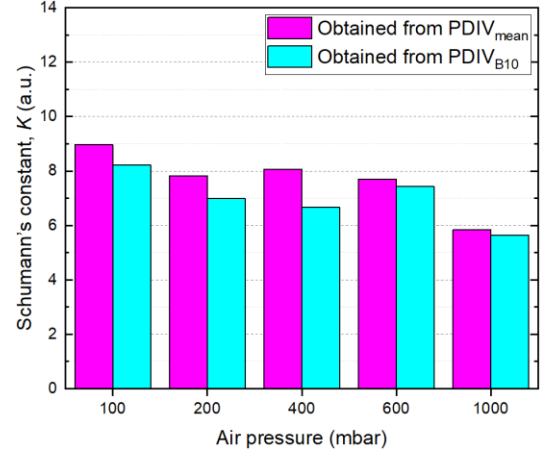


Fig. 12. K as a function of air pressure.

TABLE V
EXPERIMENTAL VALUES OF K AS A FUNCTION OF AIR PRESSURE RELEVANT TO FIG. 12.

| Air pressure (mbar) | Obtained from $\text{PDIV}_{\text{mean}}$ | | Obtained from PDIV_{B10} | |
|---------------------|---|-----------------------|--|-----------------------|
| | K (a.u.) | $p \cdot d$ (mbar.mm) | K (a.u.) | $p \cdot d$ (mbar.mm) |
| 100 | 8.97 | 89.43 | 8.22 | 91.41 |
| 200 | 7.83 | 105.15 | 6.99 | 79.84 |
| 400 | 8.07 | 83.93 | 6.68 | 97.23 |
| 600 | 7.70 | 105.33 | 7.43 | 98.36 |
| 1000 | 5.84 | 21.87 | 5.64 | 26.18 |

G. The Earliest Critical Avalanche Size (N_c)

Fig. 13 reports the earliest value of N_c with respect to air pressure from (3) directly using the K values in Fig. 12. Fig. 13 reveals that the earliest value of N_c is 22.85 and 13.3 times larger at 100 mbar than 1000 mbar, referring to $\text{PDIV}_{\text{mean}}$ and PDIV_{B10} , respectively. Also, it is 7 and 4 times greater at a cruising altitude of 11.8 km (i.e., 200 mbar) than ground level (i.e., 1000 mbar), if $\text{PDIV}_{\text{mean}}$ and PDIV_{B10} are evaluated, respectively. As a result, there is a significantly higher destructive potential of PD at reduced air pressures. Indeed, the harmfulness or damage associated with PD activity is immensely higher at low air pressures due to 1) higher energetic content of a single electron resulting from remarkably longer CFLL (Fig. 7) and 2) larger avalanche size, thus a higher number of electrons contributing to a discharge event (Fig. 13). The higher electron energies resulting from air pressure reduction are also verified in [3] using optic emission spectroscopy. Hence, PD pulses at reduced air pressures are

characterized by more abundant electrons with a higher average electron energy which can break multiple bonds or bonds inaccessible at ground level. This can explain why the corona-resistant insulations which are featured by improved behaviour at ground level are not a viable option at low air pressures since a huge number of energetic electrons can easily break the inorganic chemical bonds or the bonds between the inorganic nanoparticles and the host polymeric matrix [2]. Furthermore, Fig. 13 shows that the calculated avalanche size based on $\text{PDIV}_{\text{mean}}$ and PDIV_{B10} are close at 1000 mbar while the obtained avalanche sizes are different at reduced air pressures.

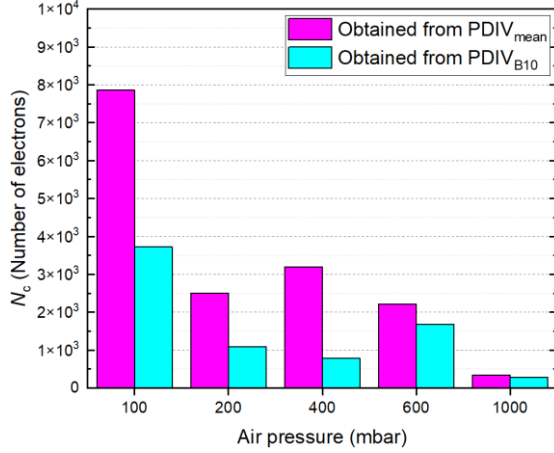


Fig. 13. Earliest value of N_c as a function of air pressure.

V. PDIV MODELLING BASED ON SCSIC

Fig. 14 displays a flowchart describing the iterative approach to predict PDIV. After determining the experimental value of K , the following iterative algorithm is employed to model PDIV [13] as a function of air pressure:

- 1) Set K to one of the following as desired:
 - 1-1 $K_{\text{mean}} = 5.840$, obtained from $\text{PDIV}_{\text{mean}}$ at 1000 mbar.
 - 1-2 $K_{\text{B10}} = 5.636$, obtained from PDIV_{B10} at 1000 mbar.
 - 1-3 $K_{\text{mean}}(p)$ introduced by (15)
 - 1-4 $K_{\text{B10}}(p)$ introduced by (16)
- 2) Import the database from COMSOL for unitary voltage. Set the primary voltage level to e.g., 100 V and calculate the electric field intensity across each field line between the two insulated wires (Fig. 1) by linearity using (9).
- 3) Import the database of ionization swarm parameters from BOLSIG+, and convert the units as explained in stage 2) of algorithm to find K . Therefore, obtain α_{eff} in mm^{-1} as a function of electric field in V/m .
- 4) Starting from the shortest field line to the longest, ascertain whether at least one field line satisfies $K \leq \int_0^{x_c} \alpha_{\text{eff}}(x) \cdot dx$, otherwise, start again from stage 3) while increasing the applied voltage.
- 5) As soon as (1) is satisfied, stop the iteration, and report the applied voltage as PDIV.

Fig. 15 illustrates the ratio of modelled and measured PDIV as a function of air pressure based on the above-mentioned K values in stage 1) of the PDIV predictive algorithm. Additionally, Table VI quantifies the PDIV estimation errors in

(%) for different used K values.

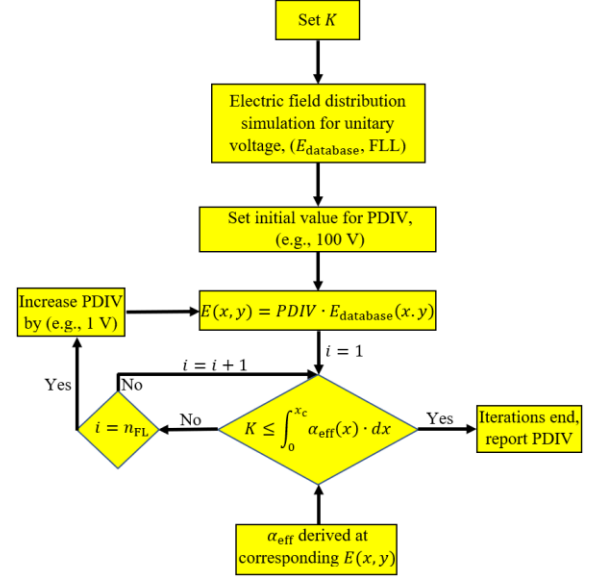


Fig. 14. A flowchart summarizing the stages in the iterative approach to predict PDIV.

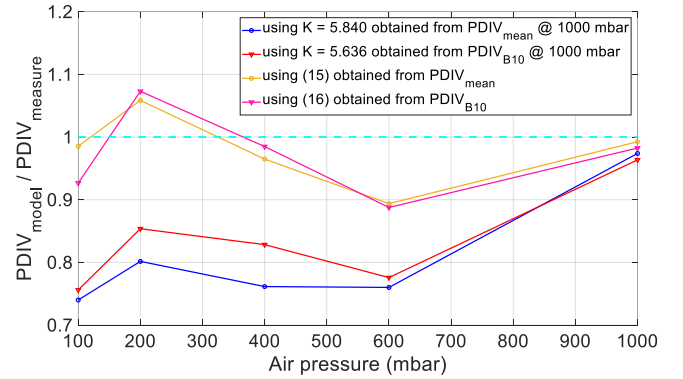


Fig. 15. The ratio of modelled and measured PDIV as a function of air pressure.

TABLE VI
PDIV PREDICTION ERROR IN (%) FOR DIFFERENT K VALUES.

| Air pressure (mbar) | 100 | 200 | 400 | 600 | 1000 |
|---------------------------|-------|--------|--------|--------|-------|
| $K_{\text{mean}} = 5.840$ | -26 | -19.84 | -23.86 | -24 | -2.62 |
| (15) | -1.47 | 5.85 | -3.52 | -10.63 | -0.75 |
| $K_{\text{B10}} = 5.636$ | -24.4 | -14.64 | -17.17 | -22.43 | -3.64 |
| (16) | -7.34 | 7.3 | -1.52 | -11.24 | -1.76 |

Fig. 15 and Table VI demonstrate that using the derived equations for K (i.e., (15) or (16)) as a function of air pressure deliver considerably lower errors in PDIV prediction at all air pressures comparing using a single K parameter value (e.g., $K_{\text{mean}} = 5.840$ or $K_{\text{B10}} = 5.636$). For example, using (15) improves the accuracy of PDIV prediction at 100 mbar about 17.7 times more than the simple approach at which a fixed value of $K_{\text{mean}} = 5.840$ is used. Moreover, using (16) instead of a single value of $K_{\text{B10}} = 5.636$ delivers 11.3 times more accurate PDIV estimation at 400 mbar. Overall, K from (15) yields the most accurate estimation of PDIV for all air pressures, except for 400 mbar, where (16) provides a more precise estimation.

VI. CONCLUSION

This contribution evaluates K as a function of air pressure and clarifies that it increases from 1000 mbar (ground level) to 100 mbar. Therefore, the obtained K at 1000 mbar (e.g., 5.84 from $PDIV_{\text{mean}}$ and 5.636 from $PDIV_{B10}$) should not be used indiscriminately to model PDIV based on SCSIC for low air pressures since delivers underestimated values. Instead, K should be introduced as a function of air pressure (e.g., $K_{\text{mean}}(p)$) to estimate K and PDIV at reduced air pressures achieving conspicuously better accuracy. In addition, it is substantiated that the N_c is significantly larger at low air pressures than that of ground level (e.g., about 23 and 7 times higher at 100 and 200 mbar, respectively, than 1000 mbar), implying the huge destructive potential of PD at reduced air pressures. This finding can explain the remarkable harmfulness associated with PD activity at low air pressures, such that even corona-resistant insulated wires alone cannot withstand PD activity [2]. Indeed, it is demonstrated that when air pressure reduces the CFLL increases significantly (e.g., about 35 and 15 times longer at 100 and 200 mbar, respectively, than 1000 mbar), reflecting a higher electric field distribution in gas rather than the solid insulation. It is revealed that α_{eff} and E_{inc} decrease drastically with air pressure reduction. This contribution reveals that, when compared to all other SIPs that exhibit considerable variations in response to air pressure, the changes in firing voltage, V_{firing} , are nearly insignificant. This remarkable observation highlights a level of stability that surpasses even the esteemed fitting parameter K , as the firing voltage remains impressively consistent amidst air pressure fluctuations. In future research to refine the model, it can be expanded by considering different environmental conditions (e.g., varying humidity and temperature levels) under reduced air pressures, along with incorporating steep-fronted waveform characteristics like rise time and switching frequency into the fitting parameter K .

REFERENCES

- [1] IEC Std. 60034-18-41, "Rotating electrical machines - part 18-41: partial discharge free electrical insulation systems (Type I) used in rotating electrical machines fed from voltage converters - qualification and quality control tests," 2019.
- [2] A. Rumi, J. G. Marinelli, D. Barater, A. Cavallini, and P. Seri, "The challenges of reliable dielectrics in modern aerospace applications: the hazard of corona resistant materials," *IEEE Transactions on Transportation Electrification*, vol. 8, no. 4, pp. 4646-4653, Dec. 2022.
- [3] A. Rumi, J. G. Marinelli, P. Seri, M. Kohler, and A. Cavallini, "Performance of corona resistant insulation for aerospace," in *2021 IEEE Electrical Insulation Conference (EIC)*, Denver, CO, USA, 2021, pp. 22-25.
- [4] A. Rumi, J. G. Marinelli, A. Cavallini, and P. Seri, "Can corona resistant wires ensure reliability in aerospace machine insulation?," in *2022 IEEE Electrical Insulation Conference (EIC)*, Knoxville, TN, USA, 2022, pp. 309-312.
- [5] M. Borghei and M. Ghassemi, "Insulation Materials and Systems for More- and All-Electric Aircraft: A Review Identifying Challenges and Future Research Needs," *IEEE Transactions on Transportation Electrification*, vol. 7, no. 3, pp. 1930-1953, Sept. 2021.
- [6] L. Lusuardi, A. Rumi, G. Neretti, P. Seri and A. Cavallini, "Assessing the severity of partial discharges in aerospace applications," in *2019 IEEE Conference on Electrical Insulation and Dielectric Phenomena (CEIDP)*, 2019, pp. 267-270.
- [7] R. Rui and I. Cotton, "Impact of low pressure aerospace environment on machine winding insulation," in *2010 IEEE International Symposium on Electrical Insulation*, San Diego, CA, pp. 1-5, 2010.
- [8] L. Lusuardi, "Towards a partial discharge free insulation system for the More Electrical Transportation," Ph.D. dissertation, University of Bologna, Bologna, Italy, Mar. 2020.
- [9] W. O. Schumann, "Über das Minimum der Durchbruchfeldstärke bei Kugelelektroden," *Arch. Elektrotech. (Berl.)*, vol. 12, pp. 593-608, 1923.
- [10] A. Pedersen, "Estimation of breakdown voltages in compressed strongly electronegative gases and gas mixtures." 1977 Conf. on Elect. Insul. and Dielectric Phenomena, 1977, pp. 380-389.
- [11] N. H. Malik, "Streamer breakdown criterion for compressed gases," *IEEE Trans. Electr. Insul.*, vol. EI-16, no. 5, pp. 463-467, Oct. 1981.
- [12] H. Raether, "Electron avalanches and breakdown in gases," *Butterworth and Co. Publishers Ltd.*, 1964.
- [13] L. Lusuardi, A. Cavallini, M. G. de la Calle, J. M. Martínez-Tarifa, and G. Robles, "Insulation design of low voltage electrical motors fed by PWM inverters," *IEEE Electr. Insul. Mag.*, vol. 35, no. 3, pp. 7-15, May-Jun. 2019.
- [14] H. Naderiallaf, P. Giangrande, and M. Galea, "Characterization of PDIV, PDEV, and RPDIV in insulated wires under unipolar repetitive square wave excitations for inverter-fed motors," *IEEE Access*, vol. 11, pp. 51047-51063, 2023.
- [15] G. J. M. Hagelaar and L. C. Pitchford, "Solving the Boltzmann equation to obtain electron transport coefficients and rate coefficients for fluid models," *Plasma Sources Sci. Technol.*, vol. 14, no. 4, pp. 722-733, 2005.
- [16] "BOLSIG+ | Electron Boltzmann equation solver." [Online]. Available: <http://www.bolsig.laplace.univ-tlse.fr/>. [Accessed: Mar. 20, 2023].
- [17] U.S. Committee on Extension to the Standard Atmosphere, "US Standard Atmosphere," National Oceanic and Atmospheric Administration, 1976.
- [18] D. Evans, J. Knaster, and H. Rajainmaki, "Vacuum Pressure Impregnation Process in Superconducting Coils: Best Practice," *IEEE Transactions on Applied Superconductivity*, vol. 22, no. 3, pp. 4202805-4202805, June 2012.
- [19] IEC Std. 60851-5, "Winding Wires—Test Methods—Part 5: Electrical Properties," 2008.
- [20] M. Goldman, A. Goldman, and J. Gatellet, "Physical and chemical aspects of partial discharges and their effects on materials," in *1993 International Conference on Partial Discharge*, 1993, pp. 11-14.
- [21] Z. Wei, H. You, P. Fu, B. Hu, and J. Wang, "Partial discharge inception characteristics of twisted pairs under single voltage pulses generated by silicon-carbide devices," *IEEE Transactions on Transportation Electrification*, vol. 8, no. 2, pp. 1674-1683, June 2022.
- [22] L. Lusuardi, A. Rumi, A. Cavallini, D. Barater, and S. Nuzzo, "Partial discharge phenomena in electrical machines for the more electrical aircraft. Part II: impact of reduced pressures and wide bandgap devices," *IEEE Access*, vol. 9, pp. 27485-27495, 2021.
- [23] L. Niemeyer, "A generalized approach to partial discharge modeling," *IEEE Trans. Dielectr. Electr. Insul.*, vol. 2, no. 4, pp. 510-528, Aug. 1995.
- [24] C. Abadie, "On-line non-intrusive partial discharge detection in aeronautical systems," Ph.D. Thesis, University of Toulouse, Toulouse, France, 2017.
- [25] A. Rumi, L. Lusuardi, A. Cavallini, M. Pastura, D. Barater, and S. Nuzzo, "Partial discharges in electrical machines for the more electrical aircraft. Part III: preventing partial discharges," *IEEE Access*, vol. 9, pp. 30113-30123, 2021.
- [26] L. Lusuardi, A. Cavallini, A. Caprara, F. Bardelli and A. Cattazzo, "The impact of test voltage waveform in determining the repetitive partial discharge inception voltage of Type I turn/turn insulation used in inverter-fed induction motors," *2018 IEEE Electrical Insulation Conference (EIC)*, San Antonio, TX, USA, 2018, pp. 478-481.
- [27] J. Gao, A. Rumi, Y. He and A. Cavallini, "Towards a holistic approach to inverter-fed machine design: FEM-based PDIV prediction of complete windings," *IEEE Transactions on Dielectrics and Electrical Insulation*, June 2023.